

Article

A Robust Vector Current Controller with Negative-Sequence Current Capability for Grid-Connected Inverters

Houshang Karimi ^{1,*}, Aboutaleb Haddadi ², Masoud Karimi-Ghartemani ³ and Mahdiah Sadabadi ⁴¹ Department of Electrical Engineering, Polytechnique Montreal, Montreal, QC H3T 1J4, Canada² Electric Power Research Institute (EPRI), Palo Alto, CA 94304, USA; ahaddadi@epri.com³ Department of Electrical and Computer Engineering, Mississippi State University, Starkville, MS 39762, USA; karimi@ece.msstate.edu⁴ Department of Automatic Control and Systems Engineering, University of Sheffield, Sheffield S1 3JD, UK; m.sadabadi@sheffield.ac.uk

* Correspondence: houshang.karimi@polymtl.ca

Abstract: This paper presents a vector current controller (in the synchronous reference, or the dq, frame) with negative-sequence current injection capability for three-phase grid-connected converters. This capability is desired for the operation of the converter during unbalanced conditions and also for a certain type of islanding detection. The proposed controller first determines the double-frequency current references and then uses a sixth-order two-input two-output proportional-integral-resonance (PIR) structure, which is optimally designed. Compared with the existing similar approaches, the proposed controller has a simpler structure and more robust performance, e.g., against system parameter uncertainties and weak grid conditions. The proposed controller is developed for converters with both the *L*-type and *LCL*-type filters. For the *LCL*-type converter, a suboptimal partial state feedback control is also proposed to achieve robust stability and active damping of resonance poles without requiring additional sensors. Detailed experimental results are presented to illustrate the properties and performances of the proposed controller.

Keywords: vector current control; distributed energy resources; grid-connected inverter; negative-sequence current injection; islanding detection



Citation: Karimi, H.; Haddadi, A.; Karimi-Ghartemani, M.; Sadabadi, M. A Robust Vector Current Controller with Negative-Sequence Current Capability for Grid-Connected Inverters. *Energies* **2021**, *14*, 4549. <https://doi.org/10.3390/en14154549>

Academic Editor: Andrea Bonfiglio

Received: 14 June 2021
Accepted: 22 July 2021
Published: 27 July 2021

Publisher's Note: MDPI stays neutral with regard to jurisdictional claims in published maps and institutional affiliations.



Copyright: © 2021 by the authors. Licensee MDPI, Basel, Switzerland. This article is an open access article distributed under the terms and conditions of the Creative Commons Attribution (CC BY) license (<https://creativecommons.org/licenses/by/4.0/>).

1. Introduction

Grid-connected converters exchange positive-sequence balanced current with the grid during normal operation. However, they may be required to exchange a negative-sequence current component in some conditions. For example, during an asymmetrical grid fault, when the grid is unbalanced [1–6] or when they are equipped with an active islanding detection mechanism, which is based on injection of a small negative-sequence current [7,8].

The common control approach is the vector current control (VCC) technique in the synchronous reference (or dq) frame where the current references become constant [9]. To maintain this desired feature of the VCC approach, i.e., having constant references, while injecting a negative-sequence current, two separate control channels are put together for each sequence component. In this approach, multiple filters must be inserted into this structure to block the double-frequency oscillations. Despite some solutions to simplify the controller, e.g., [10], this approach still has an increased order and structural complexity of the controller [7,11–13]. One more important concern with this approach is the impact of those controller dynamics in aggravating the system oscillations under weak grid conditions [14–16]. Moreover, such approaches are not directly applicable to the inverters with *LCL*-type filters due to the complex coupling of the two axes in these filters. For this reason, almost all controllers for implementing fault ride-through are structured in a stationary (or natural time) domain with extensive current reference calculations and

multiple resonance controllers [1,5,17–19]. In [20], the controller gains in a stationary frame for an *LCL*-type filter are designed using a linear matrix inequality (LMI) approach.

In [21], this problem is addressed for an inverter with an *LCL* filter where the controller and also a state observer are optimally designed. Resonant (or internal model based) controllers are used for perfect tracking. However, two different control channels are still used for the *dq* axes. In [22,23], the real power oscillations are removed by injecting an unbalanced current. However, only an *L*-type filter is considered. Separate control channels are used, and the design of current controllers are not discussed in [23].

Robust sliding mode control (SMC) for grid-connected voltage source converters (VSCs) operating under unbalanced grid conditions has been proposed in [24]. Although the proposed method does not require a phase-locked loop (PLL), it employs an observer to estimate positive- and negative-sequence components of the grid voltage. Moreover, the SMC technique suffers from the chattering phenomenon, which degrades controller performance and its accuracy [25]. In [26], an enhanced three-stage passivity-based controller for *LCL*-type VSCs connected to a weak and unbalanced grid is proposed. This method is structurally complex and assumes to have access to all current and voltage signals.

This paper proposes a new controller for a VSC based distributed energy resource (DER) unit with negative-sequence current injection capability. The application of islanding detection is considered for the study presented in this paper. The proposed controller finely determines the reference currents and then uses a multivariable proportional-integrating-resonance (PIR) function. This obviates the need for several notch filters used in existing methods, e.g., in [7,27,28], which significantly reduces the controller's order. The reduced order of the proposed controller together with its optimal design lead to a high level of robustness against weak grid conditions and system uncertainties as demonstrated in this paper. The proposed controller is applied to both *L*-type and *LCL*-type filters without requiring additional sensors or observers. The *LCL*-type filters are increasingly used due to their lower cost and volume, which leads to higher power density as well as higher efficiency for high power applications.

The effectiveness of the proposed control scheme is validated using experimental tests under IEEE1547 anti-islanding test conditions, unbalanced load, weak grid conditions, and uncertainties in the output filter parameters. All the developments and testing are performed for two cases of inverters with *L*-type and *LCL*-type output filters. Performances of the proposed method and conventional method are compared against uncertainties in system parameters and against weak grid conditions. It is shown that substantial performance improvement is achieved.

The main contributions of the paper are (1) proposing a structurally simple and robust current controller for the VSCs with negative-sequence current injection capability; (2) proposing a systematic and step-by-step control design algorithm applicable to both *L*-filter and *LCL*-filter interfaced VSCs; (3) developing an active islanding detection algorithm based on negative-sequence current injection for *L*-type as well as *LCL*-type VSCs; (4) presenting several simulation and experimental scenarios to verify the performance of the proposed control systems and islanding detection algorithm.

2. Test Setup

Figure 1 shows a schematic diagram of the test system consisting of a DER unit and a local parallel *RLC* load connected to the grid through switch *S*. The grid has been represented by an ideal voltage source behind an impedance whose per-phase resistance and inductance have been denoted by R_s and L_s . The power circuit of the DER unit comprises a conditioned prime energy source that is modeled by a dc voltage source, a VSC, and a three-phase output filter, which could be an *L*-type or *LCL*-type filter. A step-up transformer connects the DER unit to the point of common coupling (PCC). The *RLC* load is tuned at the resonance frequency of 60 ± 0.1 Hz to behave as a pure resistance, R , which is adjusted to absorb the nominal power of the DER unit at the nominal PCC voltage.

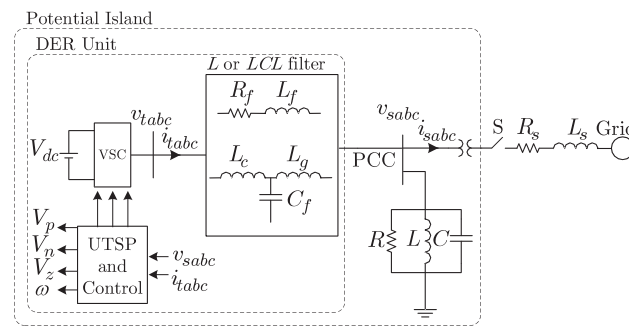


Figure 1. A schematic diagram of the test system.

3. Overview of a Conventional Islanding Detection Method

In [7], an islanding detection method is presented where the VSC injects a small amount of negative-sequence current during normal operation. Its block diagram structure is shown in Figure 2. Its current controller consists of two channels: one channel regulates the positive-sequence component of the DER terminal current and thereby the output real and reactive powers of the unit; the other channel controls the amplitude of negative-sequence current for the purpose of islanding detection. The current control task is performed in a rotating dq frame whose angle is that of the PCC voltage obtained from a PLL. A unified three-phase signal processor (UTSP) whose input is the PCC voltage is used for precise detection of negative-sequence voltage after islanding occurs.

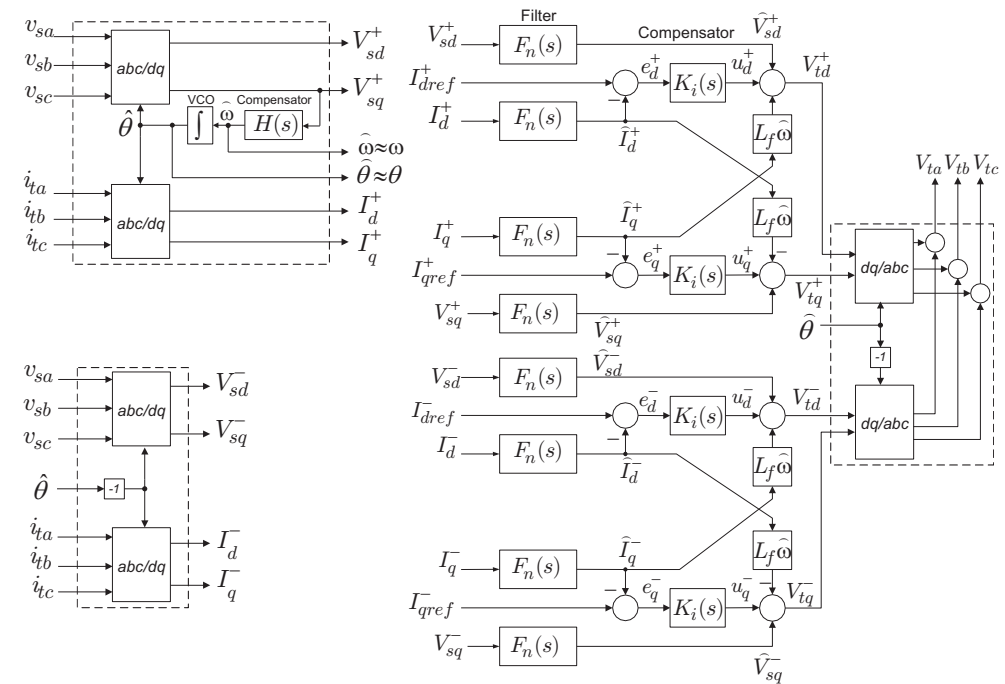


Figure 2. A schematic diagram of the conventional controller of [7].

Each control channel includes four second-order notch filters and two PI controllers. Furthermore, its PLL uses a loop filter of order 4, $H(s)$, as shown in Figure 2, in order to block the double-frequency ripples. Its UTSP is a system of order 7. The total order of the controller of [7] amounts to 30, which indicates a rather complicated structure. In addition to the implementation burden, such a complex structure causes the inverter responses to deviate from the designed characteristics when uncertain and weak grid conditions and disturbances are present, as shown in this paper.

4. Proposed Controller

As shown in Appendix B, to inject a negative-sequence current with magnitude I_n , the dq components of the current must have a double-frequency component with the same magnitude and with a 90° phase shift. Therefore, the reference values for the currents in dq frame are

$$i_{td}^*(t) = I_{td0}^* + I_n^* \cos(2\omega_0 t) \quad i_{tq}^*(t) = I_{tq0}^* - I_n^* \sin(2\omega_0 t) \quad (1)$$

where ω_0 is the nominal angular frequency.

4.1. Proposed Control Structure

The proposed control scheme directly operates on the basis of (1) and consists of an output controller and a state feedback controller, as shown in Figure 3. The output controller is a sixth-order linear time-invariant (LTI) system with two inputs and six outputs and is properly constructed (using a PIR function) so that the precise tracking of stepwise commands and double-frequency sinusoidal signals are guaranteed. Such a controller also ensures the complete rejection of dc and double-frequency disturbances. Therefore, the matrices, A_c and B_c , implement the characteristic polynomial of $p(s) = s(s^2 + 4\omega_0^2)$ in a 2I6O controllable system [29]. In other words,

$$A_c = \text{blkdiag}\{A_{c_1}, A_{c_2}\}, \quad B_c = \text{blkdiag}\{B_{c_1}, B_{c_2}\} \quad (2)$$

where blkdiag stands for “block diagonal”, and A_{c_i} and B_{c_i} are in the controllable canonical form as

$$A_{c_i} = \begin{bmatrix} 0 & 1 & 0 \\ 0 & 0 & 1 \\ 0 & -4\omega_0^2 & 0 \end{bmatrix}, \quad B_{c_i} = \begin{bmatrix} 0 \\ 0 \\ 1 \end{bmatrix}, \quad i = 1, 2 \quad (3)$$

The gains of the output controller, i.e., K_c , are multiplied with the controller state variables in a coupled manner (Figure 3). The subscript c is used for the state variables of the output controller and p for those of the plant.

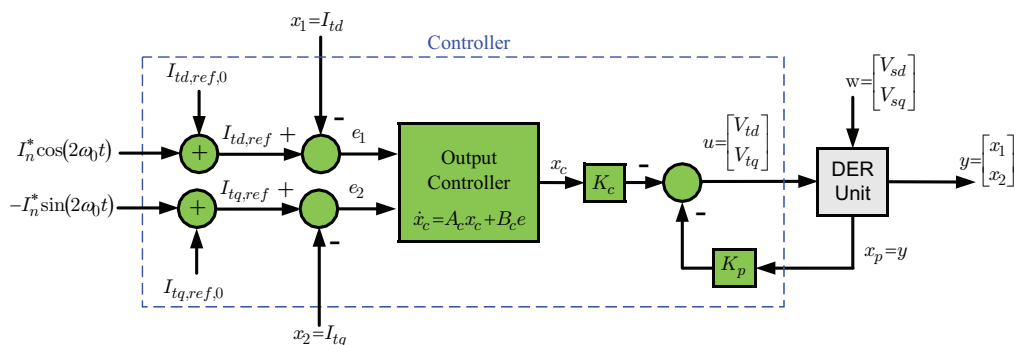


Figure 3. The structure of the proposed control scheme.

4.2. Mathematical Modeling

4.2.1. L-Type Filter

Assume the L -type filter is used with inductance L_f and parasitic resistance R_f . Moreover, let us consider the phase-angle of the PCC voltage, $\theta(t)$, as the reference phase-angle for the Park transformation. We then apply the KVL to the ac side to obtain $v_{t,dq} = R_f i_{t,dq} + L_f (\frac{di_{t,dq}}{dt} + j\omega i_{t,dq}) + v_{s,dq}$, in which $\omega = \dot{\theta}$. Defining the state, input, output, and disturbance vectors as

$$x_p^T = [x_1 \ x_2] = [i_{td} \ i_{tq}], \quad y^T = [y_1 \ y_2] = [i_{td} \ i_{tq}] \quad (4)$$

$$u^T = [u_1 \ u_2] = [v_{td} \ v_{tq}], \quad w^T = [w_1 \ w_2] = [v_{sd} \ v_{sq}],$$

leads to an LTI model described by

$$\dot{x}_p(t) = A_p x_p + B_p u + E w, \quad y = C_p x_p \quad (5)$$

$$A_p = \begin{bmatrix} -\frac{R_f}{L_f} & \omega \\ -\omega & -\frac{R_f}{L_f} \end{bmatrix}, \quad B_p = \frac{1}{L_f} I_2, \quad C_p = I_2, \quad E = -\frac{1}{L_f} I_2 \quad (6)$$

where I_2 is the 2×2 identity matrix.

The state-space model of the output controller is given by

$$\dot{x}_c = A_c x_c + B_c e = A_c x_c - B_c C_p x_p + B_c y_{ref} \quad (7)$$

where $e = y_{ref} - y = y_{ref} - C_p x_p$ is used. Augmenting the controller and plant state-space models and defining the unified state vector x as $x = [x_c^T \quad x_p^T]^T$ lead to

$$\dot{x}(t) = A x + B u + B_{ref} y_{ref} + \bar{E} w, \quad y = C x, \quad (8)$$

$$A = \begin{bmatrix} A_c & -B_c C_p \\ 0 & A_p \end{bmatrix}, \quad B = \begin{bmatrix} 0 \\ B_p \end{bmatrix}, \quad B_{ref} = \begin{bmatrix} B_c \\ 0 \end{bmatrix}, \quad \bar{E} = \begin{bmatrix} 0 \\ E \end{bmatrix}, \quad (9)$$

and $C = [0 \quad C_p]$. The control law in the form of a full state feedback may be written as

$$u = -K_c x_c - K_p x_p = -K x, \quad K = [K_c \quad K_p]. \quad (10)$$

4.2.2. LCL-Type Filter

Consider an LCL filter with the converter side impedance $L_c s + R_c$, capacitance C_f , and the grid side impedance $L_g s + R_g$. This will increase the number of plant state variables to 6, and x_p may be defined as $x_p^T = [i_{td} \quad i_{tq} \quad v_{cd} \quad v_{cq} \quad i_{gd} \quad i_{gq}]$. The plant state-space model is described by Equation (5), where the matrices are defined as

$$A_p = \begin{bmatrix} -\frac{R_c}{L_c} & \omega & -\frac{1}{L_c} & 0 & 0 & 0 \\ -\omega & -\frac{R_c}{L_c} & 0 & -\frac{1}{L_c} & 0 & 0 \\ \frac{1}{C_f} & 0 & 0 & \omega & -\frac{1}{C_f} & 0 \\ 0 & \frac{1}{C_f} & -\omega & 0 & 0 & -\frac{1}{C_f} \\ 0 & 0 & \frac{1}{L_g} & 0 & -\frac{R_g}{L_g} & \omega \\ 0 & 0 & 0 & \frac{1}{L_g} & -\omega & -\frac{R_g}{L_g} \end{bmatrix} \quad (11)$$

$$B_p^T = \frac{1}{L_c} [I_2 \quad 0], \quad C_p = [I_2 \quad 0], \quad E^T = -\frac{1}{L_g} [0 \quad I_2]$$

where 0 is the zero matrix of proper dimensions [30]. The augmented system equations and the state feedback law remain the same as Equations (8), (9), and (10), respectively.

4.3. Optimal Controller Design

The disturbances and set-points can be expressed in terms of the linear combination of dc and double-frequency sinusoidal signals, i.e., $\text{span}\{1, \cos(2\omega t), \sin(2\omega t)\}$. Therefore, applying the linear transformation defined by $p(D) = D(D^2 + 4\omega^2)$ (where D is the time derivative operator) will vanish them, i.e., $[\frac{d}{dt} (\frac{d^2}{dt^2} + 4\omega^2)] [c_1 + c_2 \sin(2\omega t) + c_3 \cos(2\omega t)] = 0$, for all constants c_1, c_2, c_3 . Now, we apply $p(D)$ to both sides of equations (8) and (10) to obtain

$$\dot{z}(t) = A z + B v, \quad \text{vs.} \quad = -K z \quad (12)$$

with $z = p(D)x = p(D) \begin{bmatrix} x_c \\ x_p \end{bmatrix} = \begin{bmatrix} z_c \\ z_p \end{bmatrix}$, and $v_s = p(D)u$. It can readily be observed that $z_c = [e_1 \dot{e}_1 \ddot{e}_1 e_2 \dot{e}_2 \ddot{e}_2]^T$ where $e_1 = i_{td,ref} - i_{td}$, $e_2 = i_{tq,ref} - i_{tq}$.

The linear quadratic regulator (LQR) technique is applied to Equation (12) to minimize

$$J = \int_0^\infty (q_1 e_1^2 + q_2 \dot{e}_1^2 + q_3 \ddot{e}_1^2 + q_4 e_2^2 + q_5 \dot{e}_2^2 + q_6 \ddot{e}_2^2 + q_7 z_{p_1}^2 + q_8 z_{p_2}^2 + r_1 v_1^2 + r_2 v_2^2) dt. \quad (13)$$

The cost function (Equation (13)) penalizes the tracking errors as well as their first- and second-order time-derivatives. All components of the cost function converge to zero if the closed-loop system is asymptotically stable.

For the LCL-type filter, the cost function is extended to

$$J = \int_0^\infty (q_1 e_1^2 + q_2 \dot{e}_1^2 + q_3 \ddot{e}_1^2 + q_4 e_2^2 + q_5 \dot{e}_2^2 + q_6 \ddot{e}_2^2 + q_7 z_{p_1}^2 + q_8 z_{p_2}^2 + q_9 z_{p_3}^2 + q_{10} z_{p_4}^2 + q_{11} z_{p_5}^2 + q_{12} z_{p_6}^2 + r_1 v_1^2 + r_2 v_2^2) dt. \quad (14)$$

A step-by-step algorithm for designing the state feedback gains is proposed as follows.

Design Algorithm for L-Type Filter:

- Step 1.** Initialize the parameters of the cost function to $r_1 = r_2 = 1$ and $q_1 = q_4 = \epsilon$, where $0 < \epsilon \ll 1$ is a real number, and the remainder of q_i 's are zero.
- Step 2.** Increase q_1 and calculate K using the MATLAB command `lqr`. Plot the trajectory of closed-loop poles, i.e., eigenvalues of $A_{cl} = A - BK$. Increase q_1 until the low-frequency dominant poles obtain sufficient distance from the imaginary axis. Freeze q_1 and proceed to Step 3.
- Step 3.** Repeat Step 2 for q_4 . This will shift the low-frequency poles of the second channel to the left.
- Step 4.** Repeat Step 2 consecutively for q_2 , q_5 , q_3 , and q_6 . Notice that q_2 and q_3 are the coefficients of the \dot{e}_1 and \ddot{e}_1 , and this means that they can introduce more damping to the high-frequency poles (at double-frequency). The same is true for q_5 and q_6 of the second control channel.
- Step 5.** Final fine-tuning may be carried out by increasing q_7 and q_8 until the closed-loop poles are located at desirable places.

Design Algorithm for LCL-Type Filter:

- Step 1–4.** Same as for the L-type filter.
- Step 5.** Increase q_7 , q_8 , and q_9 , consecutively, to introduce sufficient damping to the resonance poles of the LCL
- Step 6.** Final fine-tuning may be carried out by increasing q_{10} to q_{12} until the closed-loop poles are located at desirable places.

Remark on distance of poles: The distance of the closed-loop poles from the imaginary axis determines the speed of responses. This distance should be sufficient to produce fast responses that ensure current limiting is achieved when grid voltage transient faults occur. However, on the other side, the distance is limited by the measurement noise sensitivity and also the switching frequency constraints, i.e., the common rule that several switching cycles must be included within the time constant of the system responses.

Design Example for L-Type Filter:

Figure 4 shows the loci of the closed-loop system poles obtained by executing the proposed design algorithm. The numerical values of the system parameters are given in Table A1. In this figure, first, q_1 varies from 10^{14} to 10^{18} . The loci of the poles versus the variations of q_1 are shown in blue. Then, q_4 varies from 10^{14} to 10^{18} , and the movement of the poles is shown in red. Subsequently, q_2 and q_5 vary between 10^{10} to $10^{12.5}$, consecutively. Finally, q_3 and q_6 are varied between 10^4 to $10^{6.5}$. These introduce adequate damping to the double-frequency poles of the controller. At this location, the closed-loop system poles

are at $-458 \pm j345$, $-364 \pm j125$, $-346 \pm j987$, and $-243 \pm j831$, which indicates fast and damped responses. The controller gains are

$$K = \left[\begin{array}{cccccc|cc} -9.7 \times 10^8 & -3.2 \times 10^5 & -4976 & 2.6 \times 10^8 & 9.3 \times 10^4 & 1395 & 7 & 0 \\ -2.6 \times 10^8 & -9.3 \times 10^5 & 1395 & -9.7 \times 10^8 & -3.2 \times 10^5 & -4976 & 0 & 7 \end{array} \right]$$

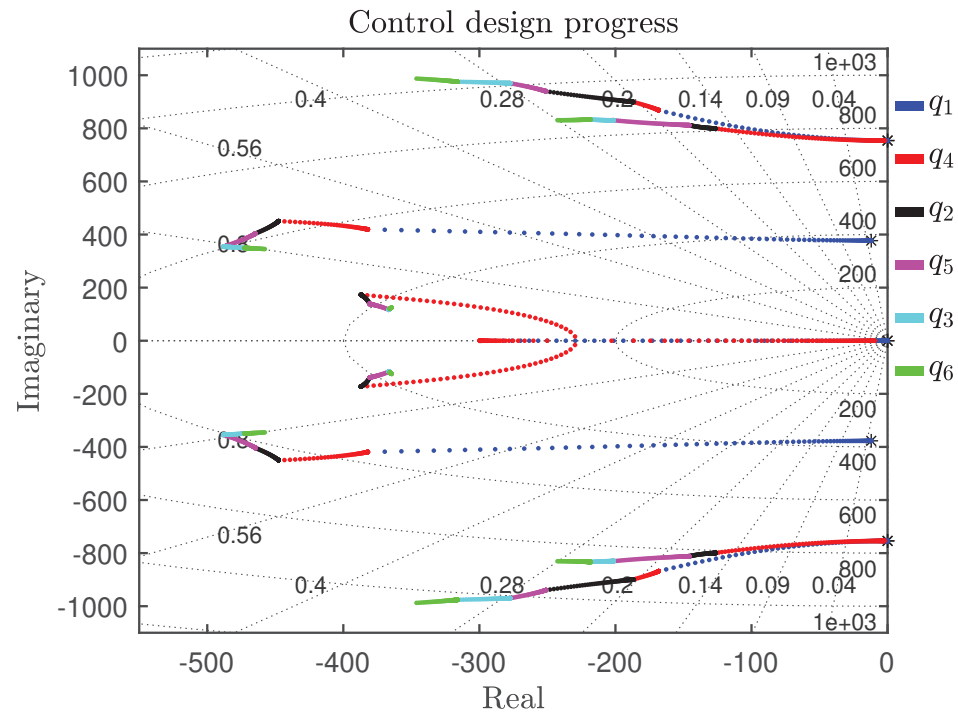


Figure 4. Loci of the closed-loop system poles for the L-type filter.

Design Example for LCL-Type Filter:

Figure 5 shows the loci of the poles of the closed-loop system when the proposed design algorithm is executed for the LCL-type filter. First, q_1 and q_4 are consecutively increased from 10^{15} to 10^{18} . Subsequently, q_2 and q_5 are varied between 10^9 to $10^{12.5}$. Then, q_3 and q_6 are varied between 10^3 and $10^{6.5}$. These introduce adequate damping to the double-frequency poles of the controller. Finally, q_7 and q_8 are varied between 10^{-2} and 10^1 ; q_9 and q_{10} are increased from 10^{-3} to 10^{-1} . This will introduce sufficient damping to the resonance poles. At this location, the closed-loop poles are at $-414 \pm j361$, $-395 \pm j4966$, $-395 \pm j4212$, $-248 \pm j66$, $-236 \pm j862$, and $-143 \pm j780$, which indicates fast and damped responses. The controller gains are

$$K = \left[\begin{array}{cccccc|cccccc} -9.3 \times 10^8 & 6.7 \times 10^5 & -4.8 \times 10^3 & 3.8 \times 10^8 & -2.2 \times 10^5 & 1.7 \times 10^3 & 8.95 & 0 & 0.14 & -0.02 & 1.44 & -0.14 \\ -3.8 \times 10^8 & 2.2 \times 10^5 & -1.7 \times 10^3 & -9.3 \times 10^8 & 6.7 \times 10^5 & -4.8 \times 10^3 & 0 & 8.95 & 0.02 & 0.14 & 0.14 & 1.44 \end{array} \right]$$

Design for LCL-Type Filter without Additional Sensors:

The LCL-type filter requires six additional number of sensors compared with the L-type filter. The proposed optimal controller design, however, proved to be working without using the new state variables of the LCL-type filter in the feedback loop. Figure 6 shows the closed-loop eigenvalues of the system when the gains of the additional signals are forced to zero. It is observed that this does not introduce instability or noticeable performance degradation, compared to when all the variables are used in the feedback, i.e., Figure 5. The

closed-loop poles are at $-478 \pm j4152$, $-440 \pm j4912$, $-277 \pm j379$, -240 ± 140 , $-237 \pm j927$, and $-136 \pm j796$, which indicates fast and damped responses. The controller gains are

$$K = \underbrace{\begin{bmatrix} -9.4 \times 10^8 & 6.6 \times 10^5 & -4.8 \times 10^3 & 3.5 \times 10^8 & -2.1 \times 10^5 & 1.6 \times 10^3 \\ -3.5 \times 10^8 & 2.1 \times 10^5 & -1.6 \times 10^3 & -9.4 \times 10^8 & 6.6 \times 10^5 & -4.8 \times 10^3 \end{bmatrix}}_{K_c} \underbrace{\begin{bmatrix} 8.84 & 0 & 0 & 0 & 0 & 0 \\ 0 & 8.84 & 0 & 0 & 0 & 0 \end{bmatrix}}_{K_p}$$

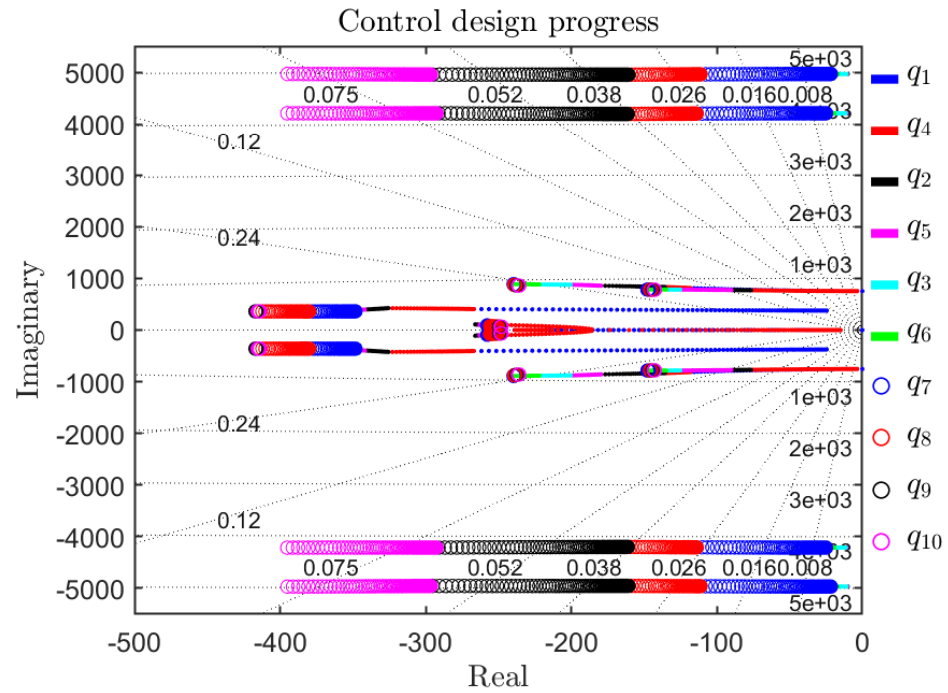


Figure 5. Loci of the closed-loop system poles for the LCL-type filter.

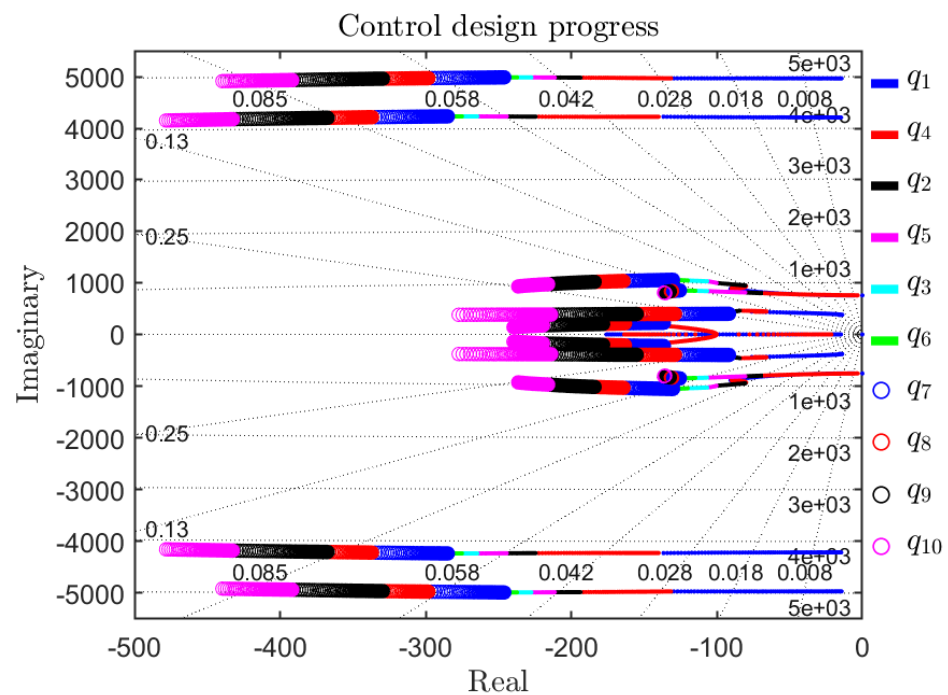


Figure 6. Loci of the closed-loop system poles for the LCL-type filter without additional sensors.

4.4. Detection of Sequences

A modified version of the unified three-phase signal processor (UTSP) of [7] is used in this paper. This was recently proposed in [22]. It is capable of robustly and accurately measuring the negative-sequence voltage. The operation of this processor is conveniently controlled by two gains: μ_1 and μ_2 . The setting of these two gains are $\mu_1 = \frac{2}{3}(2\zeta_1\omega)$, $\mu_2 = \frac{2}{3}\frac{\mu_1^2}{4\zeta_2^2}$, where ζ_1 and ζ_2 are two damping ratios. The first damping ratio specifies the filtering strength, while the second damping ratio determines the bandwidth of the frequency estimation loop.

5. Robust Stability Analysis

It is shown that multivariable quadratic designs have the property of a large gain margin and good phase margin for each control loop. Similar results are derived for nonlinear perturbations in the feedback loop [31,32]. However, in this section, a robust stability analysis for the closed-loop system with respect to uncertainties in the system parameters is carried out. The state-space A-matrix of the closed-loop system is $A_{cl} = A - BK$, where the state feedback gain K is designed in Section 4.3. To incorporate the parameter uncertainties, an approach is to employ a matrix set, referred to as the polytopic uncertain matrix, as described in [33]

$$A_{cl}(\lambda) = \sum_{i=1}^q \lambda_i A_{cl_i}, \quad (15)$$

where A_{cl_i} , $i = 1, \dots, q$, are known vertices of the polytope; q is the number of vertices; $\lambda = [\lambda_1 \dots \lambda_q]^T$ belongs to a standard unit simplex defined by

$$\Lambda = \left\{ \lambda : \lambda_i \in \mathbb{R}, \lambda_i \geq 0, \sum_{i=1}^q \lambda_i = 1 \right\}. \quad (16)$$

Theorem 1. *The closed-loop state matrix in Equation (15) is stable for all $\lambda \in \Lambda$ if there exist symmetric positive-definite matrices $P_i \succ 0$ ($i = 1, \dots, q$), S_1 , and S_2 such that*

$$\begin{bmatrix} 0 & P_i \\ P_i & 0 \end{bmatrix} + \begin{bmatrix} S_1 \\ S_2 \end{bmatrix} [I \quad -A_{cl_i}] + \left(\begin{bmatrix} S_1 \\ S_2 \end{bmatrix} [I \quad -A_{cl_i}] \right)^T \prec 0, \quad (17)$$

for $i = 1, \dots, q$.

Proof. See Theorem 2.4 in [34]. \square

The conditions given in Equation (17) are in terms of LMIs in unknown variables P_i , S_1 , and S_2 . The LMIs can be solved using YALMIP [35] as an interface and MOSEK [36] as a semidefinite programming (SDP) solver.

5.1. Robust Stability Analysis for L-Type Filter

To analyze the robust stability of the closed-loop system with respect to the uncertainty in the VSC and grid inductances, i.e., L_f and L_s , which are connected in series, it is assumed that $L_f + L_s \in [L_{\min} \quad L_{\max}]$. In this case, the polytope in Equation (15) has $q = 2$ vertices:

$$\begin{aligned} A_{cl_1} &= A(L_{\max}) - B(L_{\max})K, \\ A_{cl_2} &= A(L_{\min}) - B(L_{\min})K, \end{aligned} \quad (18)$$

where $(A(L_{\max}), B(L_{\max}))$, and $(A(L_{\min}), B(L_{\min}))$ are obtained from Equation (9) by substituting the maximum and minimum values of $L_f + L_s$, respectively. The values of L_{\min} and L_{\max} are initially chosen close to the nominal value of L_f . Subject to the

feasibility of the LMI conditions in Equation (17), the uncertainty interval $[L_{\min} \ L_{\max}]$ is iteratively stretched such that the largest possible uncertainty interval is found. Following this procedure, the uncertainty interval $L_f + L_s \in [1 \ 35]$ -mH is obtained. As a result, the LMI conditions in equation (17) guarantees that the closed-loop system is robustly stable for all values of $L_f + L_s$ in the given interval.

5.2. Robust Stability Analysis for LCL-Type Filter

For the case of the LCL-type filter, the robust stability of the closed-loop system is analyzed for the uncertainties in the LCL filter parameters L_c , L_g , C_f , and the grid inductance L_s . In this case, the polytope in Equation (15) has $q = 2^3$ vertices A_{cl_i} , $i = 1, \dots, q$, obtained by substituting the maximum and minimum values of L_c , $L_g + L_s$, and C_f in the plant model (Equation (11)) and the resultant matrices in Equation (9). Following the stretching procedure proposed for the case of the L-type filter, the robust stability of the closed-loop system for all values of L_c , $L_g + L_s$, and C_f in the intervals $L_c \in [1 \ 17.5]$ -mH, $L_g + L_s \in [2.5 \ 15]$ -mH, and $C_f \in [10 \ 22]$ - μ F is guaranteed.

6. Performance Evaluation

An experimental test setup has been developed, as shown in Figure 7, with the parameters of Table A1. This realizes the test system of Figure 1 and is a hardware-in-the-loop (HIL) configuration consisting of: (1) a 20-kVA two-level SemikronSKHI61 inverter; (2) a pulse width modulation (PWM) signal generator; (3) either an L-type filter realized by a 5-mH, 25-A inductor or an LCL-type filter realized by two 5-mH, 25-A inductors and a 19- μ F capacitor; (4) a 20-kVA, 50:120 V step-up transformer; (5) a dc voltage source implemented using a full-bridge diode rectifier fed by a 24.2-kVA, 50-A autotransformer with a variable output voltage of 0–280 V, a 450-V dc capacitor on the dc side of the diode rectifier, and a 1:1 isolating transformer interfacing the ac side of the diode rectifier to the grid; (6) a circuit breaker (CB) representing the islanding switch; and (7) an RLC load connected to the low-voltage side of the step-up transformer. The DER controller is implemented on an OP5600 real-time digital simulator. The simulator and the hardware interact through: (i) an OP8660 HIL Controller and Data Acquisition Interface that measures v_{abc} , V_{dc} , and i_{tabc} signals and supplies them to the OP5600 simulator; and (ii) three output channels of the OP5600 simulator that supply the reference signals v_{tabc}^* to the PWM signal generator device. The amplitude of the injected negative-sequence current has been fixed at 4%, and the detection threshold is set at 2%. All signals are saved using OP5600 scopes as data files and then re-plotted in MATLAB.

6.1. L-Type Filter

6.1.1. Performance Under the IEEE1547 Test Conditions

This standard requires the DER unit to detect the island within 2 s of its formation. At $t = 1$ s, an intentional islanding event is produced by manually opening the circuit breaker CB. Figure 8 presents the results. The DER detects this increase in V_n and successfully declares an islanding condition within about 6 ms. Figure 8c shows the injected double-frequency perturbations in I_{td} and I_{tq} . Figure 8e,g show that V_p and f have the same steady-state value before and after the islanding event since the DER powers match those of the load in steady-state.

6.1.2. Effect of Load (L) Imbalance

In this case, the inductance of phase ‘a’ of the load has been reduced by 50%. Figure 9 shows that the proposed control scheme maintains stability and detects the island in about 4 ms. Contained oscillations in V_n are due to the resonance between the perturbed L and C. This mismatch also causes the frequency to deviate from its nominal value following the islanding.

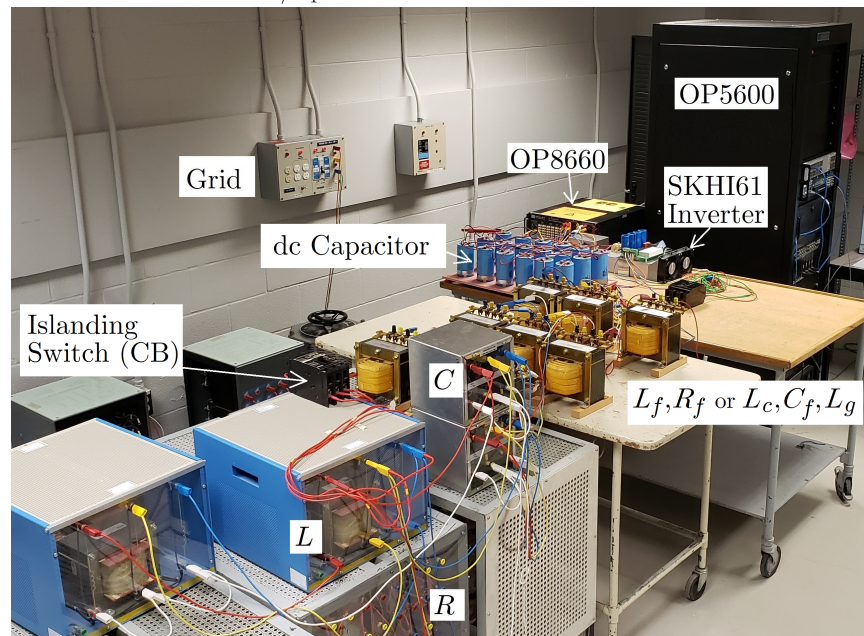
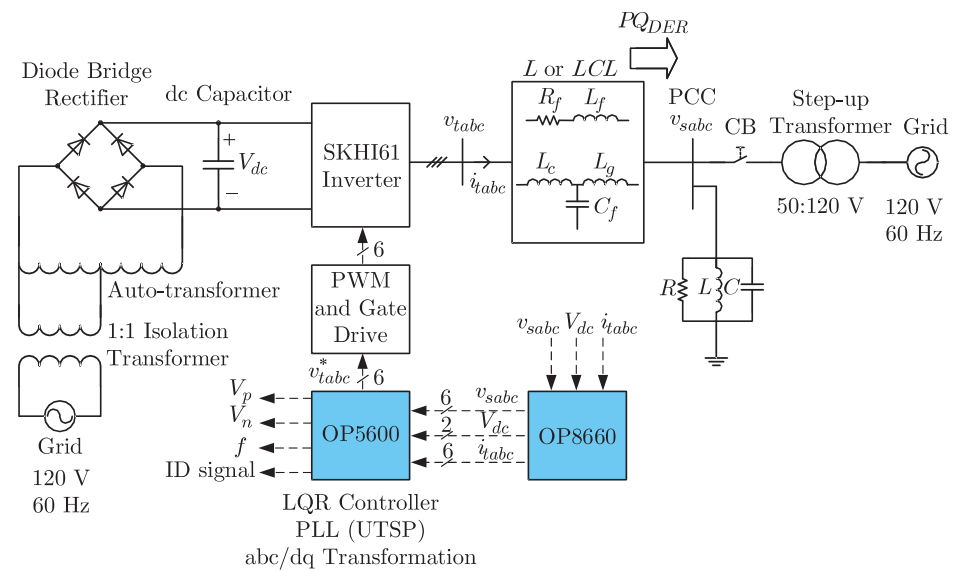


Figure 7. Experimental setup: (top) a block diagram of the circuit, and (bottom) the laboratory setup.

6.1.3. Performance Under Weak Grid Conditions

The PCC short-circuit ratio (SCR) is weakened by adding a 5-mH series inductor between the PCC and the low-voltage terminals of the step-up transformer. Before adding this inductor, the PCC SCR is about 10, and the added 5-mH inductor reduces the SCR to about 1.8, thus creating a weak grid condition. Figure 10 illustrates the stable performance of the control and the successful detection of the island within about 2 ms.

6.1.4. Effect of Filter Parameter Uncertainty

The inductance of the output filter has been increased by 100% by adding another 5-mH inductor to it. Figure 11 illustrates the stable performance of the controller and the successful detection of the island in about 7 ms despite this considerable uncertainty.

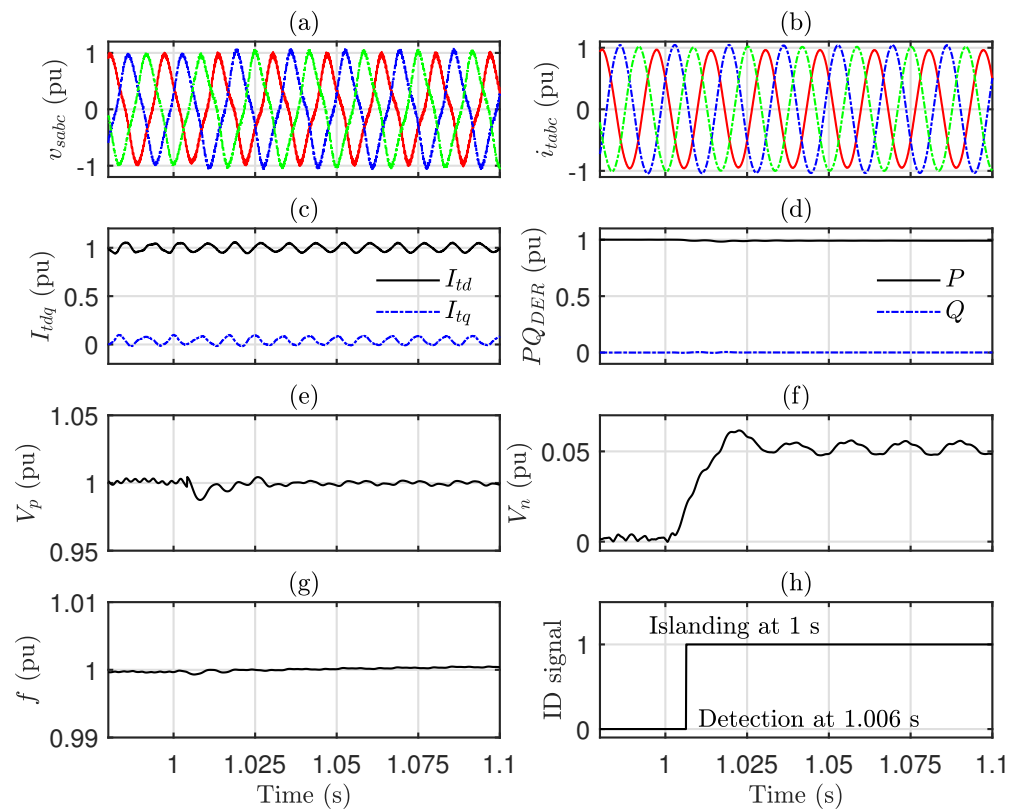


Figure 8. *L*-type filter case: Performance of the proposed controller under the IEEE1547 anti-islanding test: (a) three-phase PCC voltages; (b) three-phase inverter terminal currents; (c) *d*- and *q*-axis components of the inverter terminal current; (d) fundamental frequency power components of the DER unit; (e,f) amplitudes of positive- and negative-sequence PCC voltage, respectively; (g) frequency; and (h) ID signal.

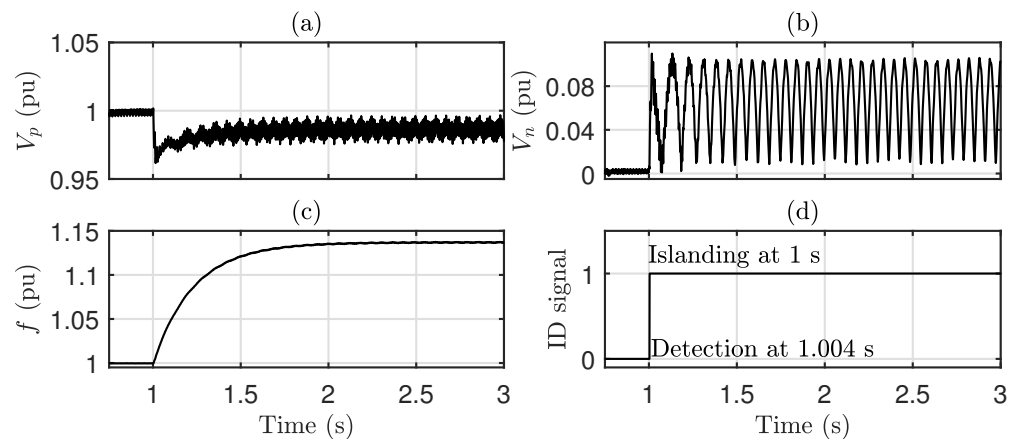


Figure 9. *L*-type filter case: Performance under load (*L*) imbalance: (a,b) estimated magnitudes of positive- and negative-sequence PCC voltage, respectively; (c) estimated frequency; and (d) ID signal.

6.2. LCL-Type Filter

6.2.1. IEEE1547 Test Conditions

Figure 12 illustrates the successful detection of the islanding event in about 5 ms.

6.2.2. Load (*L*) Imbalance

Figure 13 shows the successful detection of the islanding event in about 4 ms.

6.2.3. Weak Grid Conditions

Figure 14 shows that the controller has a stable performance, and the islanding detection is successful under weak grid conditions. The pre-islanding negative-sequence voltage component at PCC appears but does not cause an erroneous islanding detection.

6.2.4. Filter Parameter Uncertainty

The grid-side inductance of the *LCL* filter has been increased by 100% by adding a 5-mH inductor in the series with L_g . Figure 15 shows the results illustrating the stable performance of the controller and the successful detection of the island in about 4 ms.

6.3. Comparison with Conventional Controller

The conventional controller is designed according to the guidelines of [7]. The parameters of the system and controller are given in Table I and Appendix A of [7]. At $t = 1$ s, a step jump from 0.66 pu (2300 A) to 1 pu (3460 A) in the positive-sequence real current is applied to both systems. The following four scenarios are simulated in the MATLAB/Simscap environment using the realistic switching model of the VSC. In each scenario, the real and reactive currents, and the error of the current signals for both conventional and proposed systems are shown.

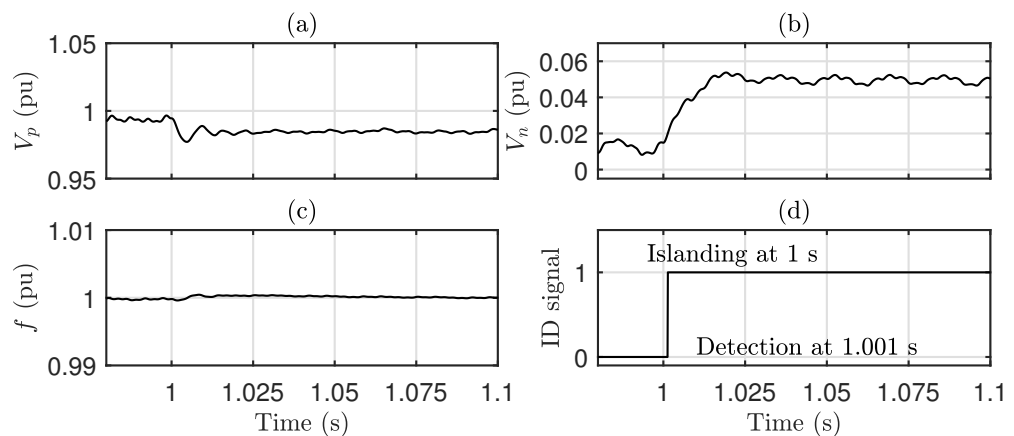


Figure 10. *L*-type filter case: Performance under weak grid condition with SCR = 1.8: (a,b) estimated magnitudes of positive- and negative-sequence PCC voltage, respectively; (c) estimated frequency; and (d) ID signal.

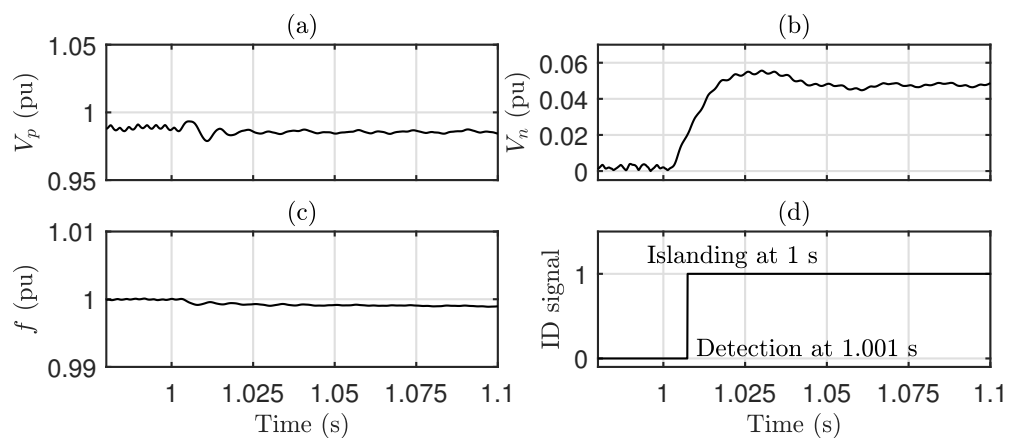


Figure 11. *L*-type filter case: Performance under 100% increase in filter inductance: (a,b) estimated magnitudes of positive- and negative-sequence PCC voltage, respectively; (c) estimated frequency; and (d) ID signal.

6.3.1. Case I: Base Conditions

In this case, no uncertainty is considered, and the grid is stiff ($SCR = 20$). Figure 16 shows that both methods have similar transient responses, while the proposed one shows better decoupling of the real and reactive currents.

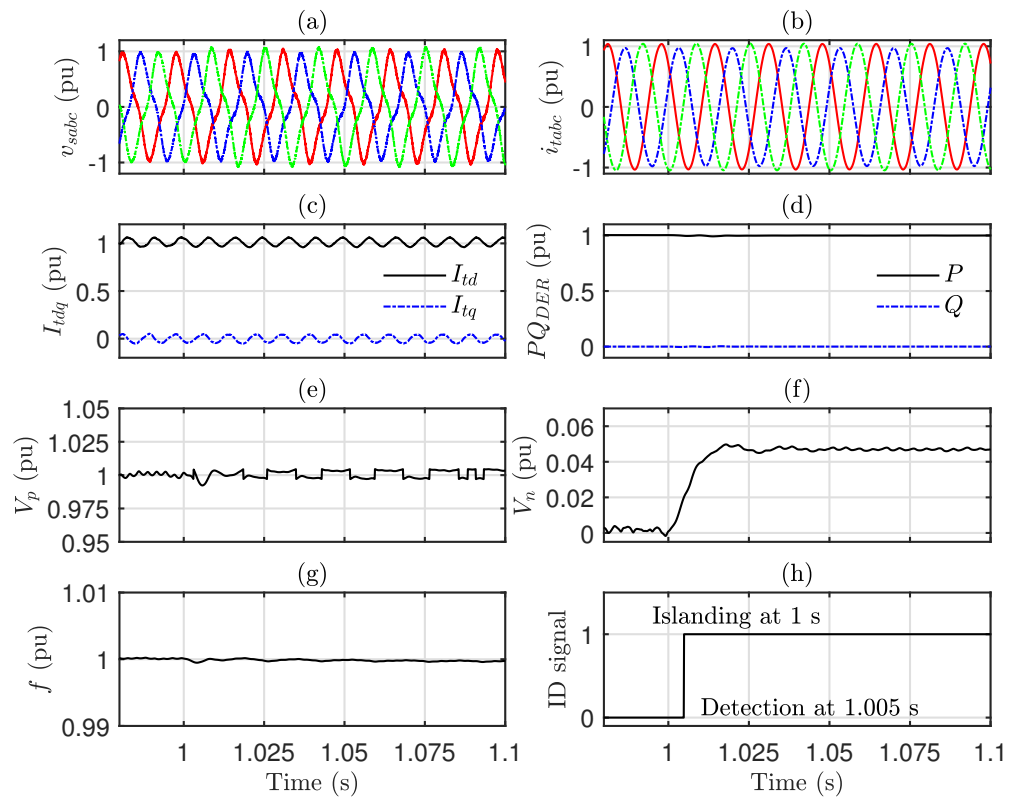


Figure 12. LCL-type filter case. Performance of the proposed controller under the IEEE1547 anti-islanding test: (a) three-phase PCC voltages; (b) three-phase inverter terminal currents; (c) d - and q -axis components of inverter terminal current; (d) fundamental frequency power components of the DER unit; (e,f) amplitude of positive- and negative-sequence voltages at PCC, respectively; (g) frequency; and (h) ID signal.

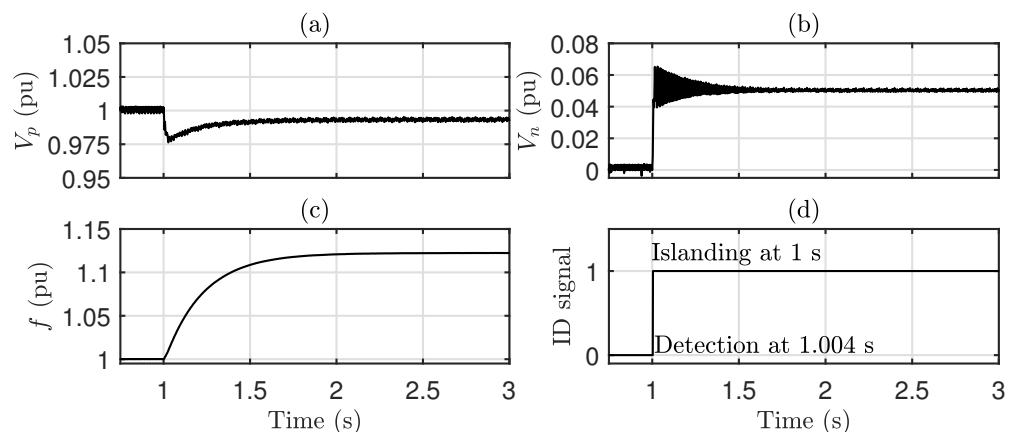


Figure 13. LCL-type filter case. Performance under load (L) imbalance: (a,b) estimated magnitudes of positive- and negative-sequence PCC voltage, respectively; (c) estimated frequency; and (d) ID signal.

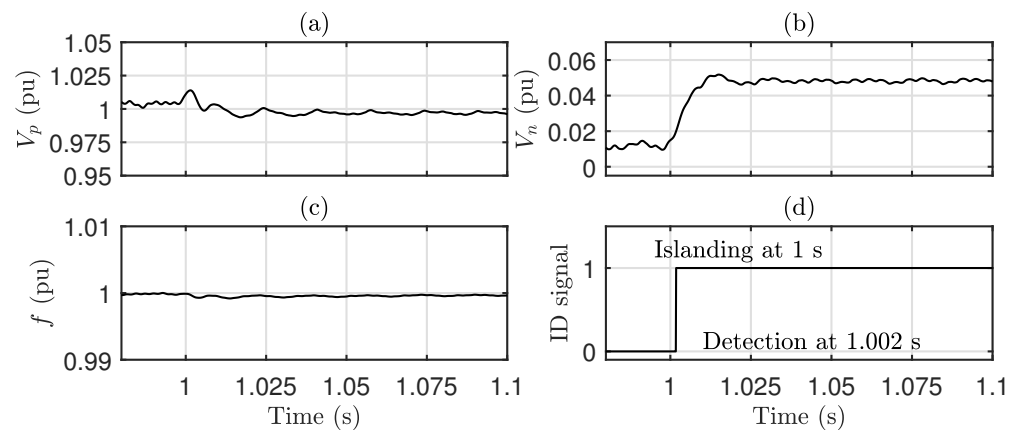


Figure 14. *LCL*-type filter case. Performance under weak grid condition with $SCR = 1.8$: (a,b) estimated magnitudes of positive- and negative-sequence PCC voltage, respectively; (c) estimated frequency; and (d) ID signal.

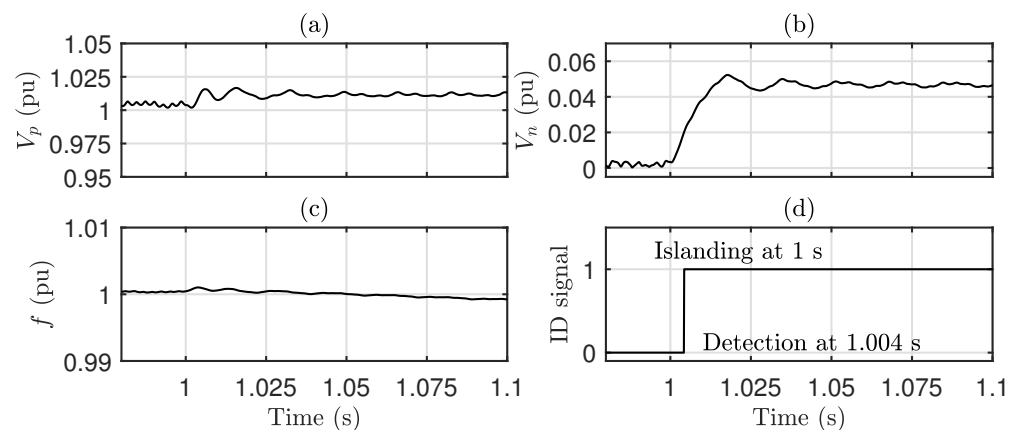


Figure 15. *LCL*-type filter case: Performance under 100% increase in L_g : (a,b) estimated magnitudes of positive- and negative-sequence PCC voltage, respectively; (c) estimated frequency; and (d) ID signal.

6.3.2. Case II: Uncertain Conditions

An uncertainty of 30% is introduced in the inverter filter inductance. Figure 17 shows that this uncertainty has slowed down the conventional method's response, while the proposed method is unaffected.

6.3.3. Case III: Weak Grid Conditions

A weak grid condition that reduces the SCR from 20 to 2 is introduced in the system. Figure 18 shows that this weak grid condition has caused a further increase in the response transient time and the level of oscillations in the conventional method, while the proposed method is unaffected.

6.3.4. Case IV: Uncertain and Weak Grid Conditions

A 50% uncertainty in the filter inductance is combined with the weak grid condition ($SCR = 2$). Figure 19 shows that the responses of the conventional system have become very sluggish, and the coupling between the real and reactive current loops has increased, whereas the proposed method is still unaffected.

Further simulations demonstrate that the proposed method is strongly robust against the inverter filter uncertainties and weak grid conditions. For example, with an uncertainty of 250% in the inverter filter combined with an extremely weak grid ($SCR = 1$), the proposed method still provides good performance, while the conventional system shows poor performance and even becomes unstable when the uncertainty in the L -filter exceeds

100% and the grid SCR is below two. This concludes that due to the inclusion of multiple additional filters in the conventional controller, interfering dynamics are produced, which compromise its robust performance and stability under uncertain and/or weak grid conditions. Moreover, the proposed method is computationally more efficient than the conventional method. For example, when running the simulation in the Matlab/Simulink at the same conditions, the conventional method takes about twice more time than the proposed method.

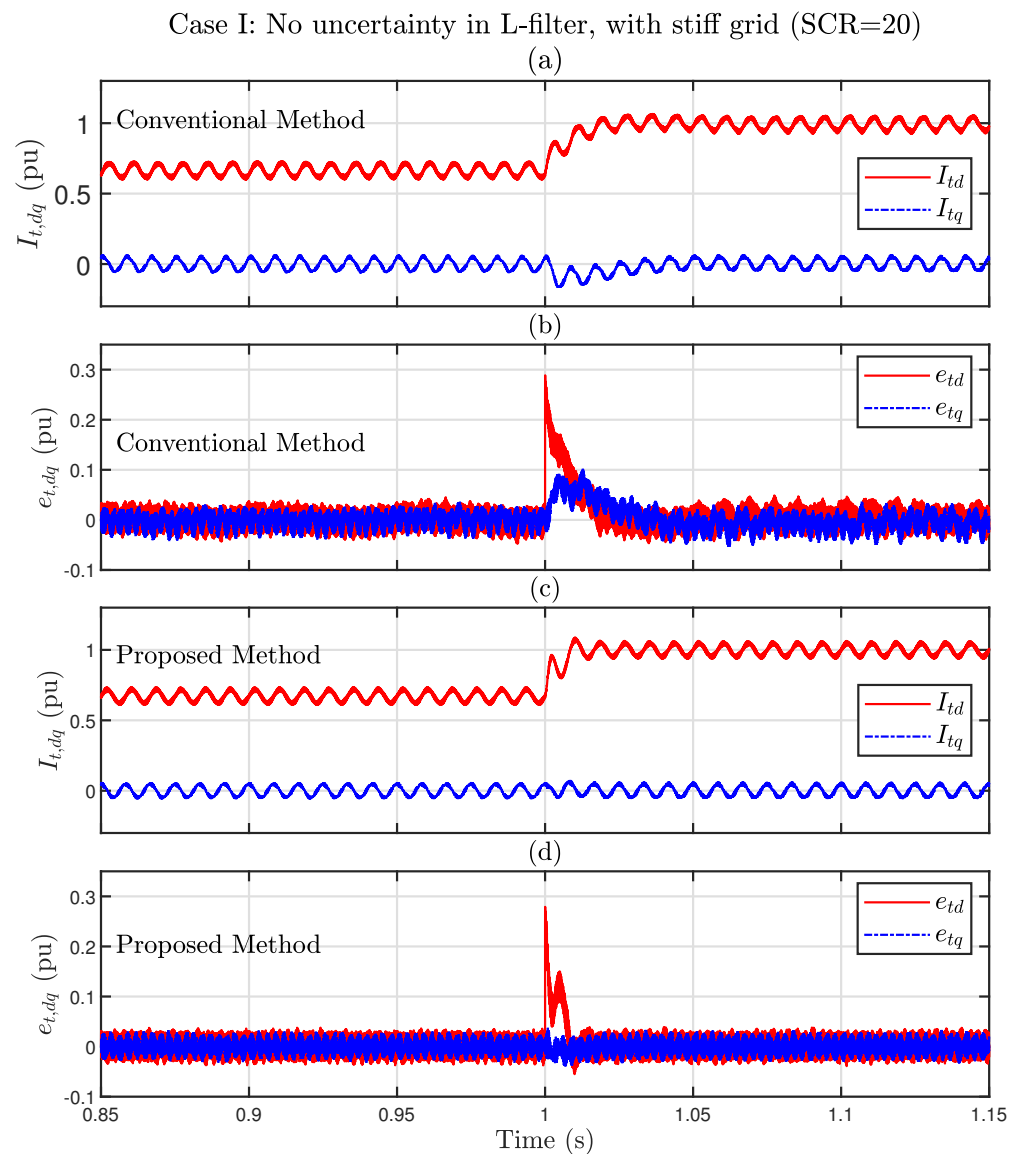


Figure 16. Comparison of the results for Case I: dq components of the inverter currents ($I_{t,dq}$) and error signals ($e_{t,dq}$): (a,b) conventional method, and (c,d) proposed method.

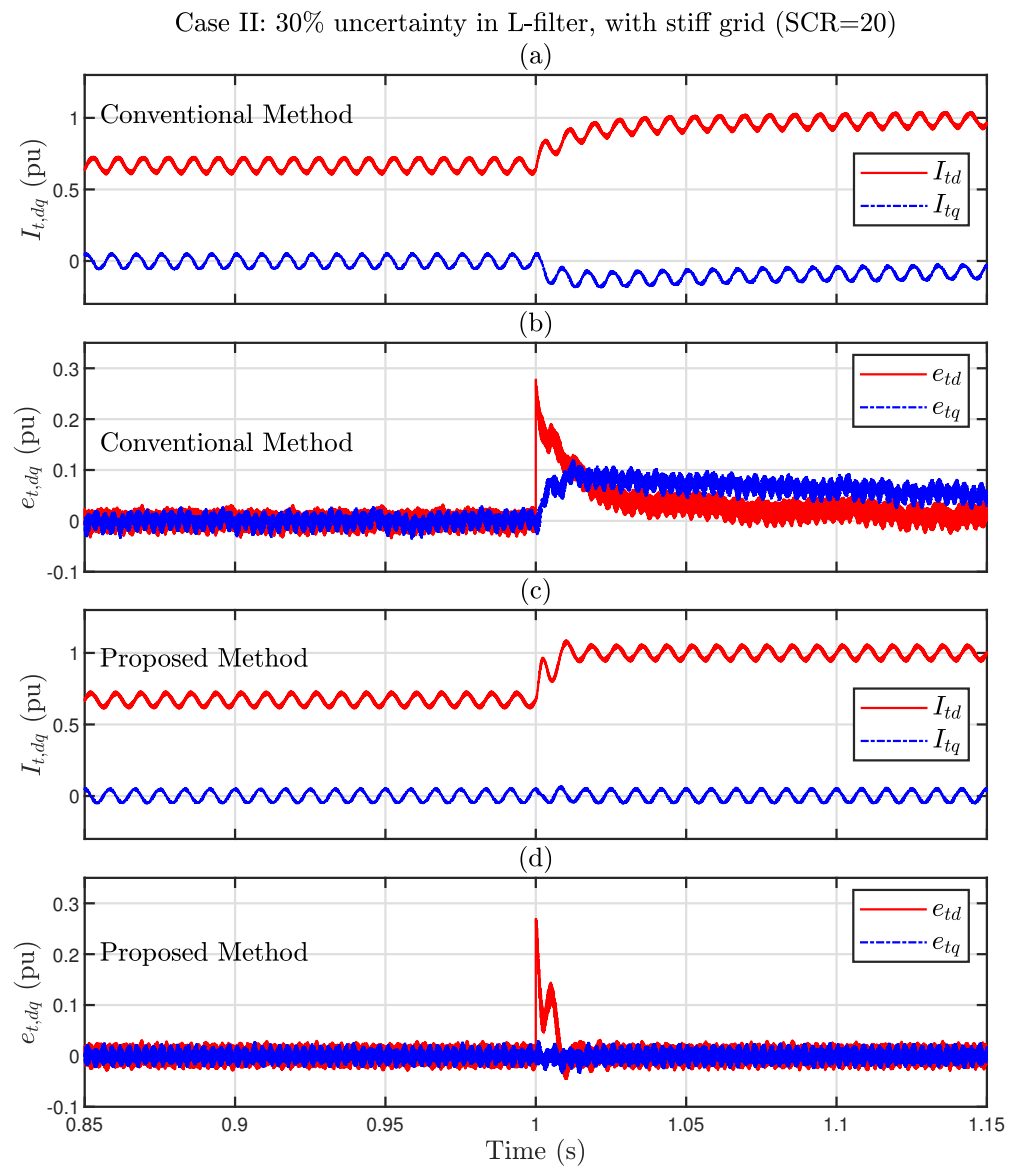


Figure 17. Comparison of the results for Case II: dq components of the inverter currents ($I_{t,dq}$) and error signals ($e_{t,dq}$): (a,b) conventional method, and (c,d) proposed method.

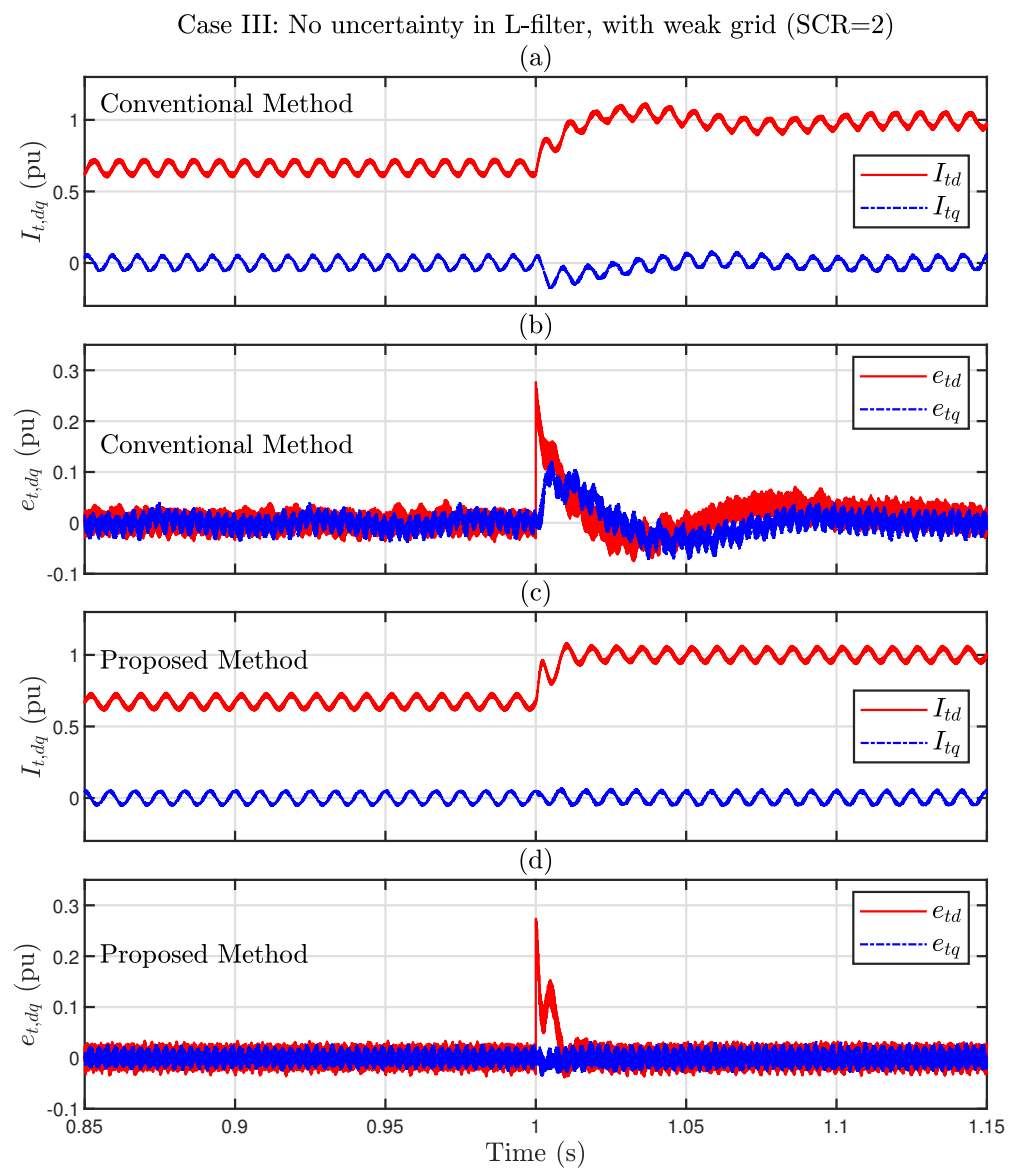


Figure 18. Comparison of the results for Case III: dq components of the inverter currents ($I_{t,dq}$) and error signals ($e_{t,dq}$): (a,b) conventional method, and (c,d) proposed method.

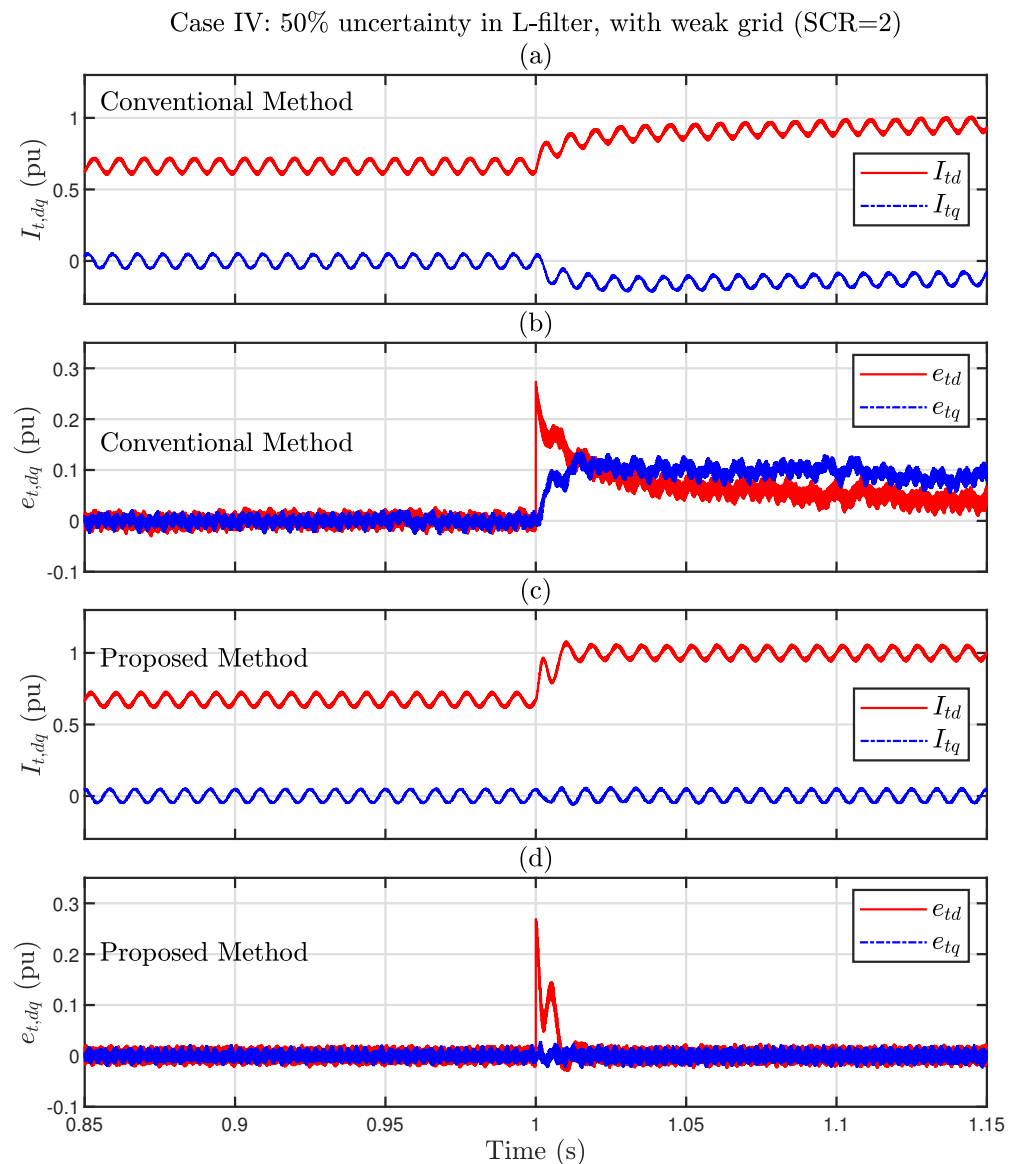


Figure 19. Comparison of the results for Case IV: dq components of the inverter currents ($I_{t,dq}$) and error signals ($e_{t,dq}$): (a,b) conventional method, and (c,d) proposed method.

7. Conclusions

This paper presented a new controller for a grid-connected converter unit with negative-sequence current capability. The main advantage of the proposed control scheme with respect to the similar existing one is the simultaneous control of the negative-sequence perturbation and positive-sequence current by means of a single unified controller. This feature greatly simplifies the controller. This simplified structure, together with the optimal design of the proposed control scheme, provides a high level of robustness against variation of grid stiffness and filter parameter uncertainties. The proposed controller is also applicable to both L - and LCL -type output filters.

Author Contributions: Conceptualization, H.K. and M.K.-G.; Modeling and simulation, H.K. and A.H.; Experimental results, A.H., M.K.-G., and H.K.; Formal analysis, H.K., M.K.-G., M.S.; Stability analysis, M.S.; Investigation, H.K., A.H., and M.K.-G.; Writing—original draft preparation, A.H. and M.K.-G.; Writing—review and editing, M.K.-G., A.H., and H.K.; Supervision, H.K. and M.K.-G. All authors have read and agreed to the published version of the manuscript.

Funding: This research received no external funding.

Conflicts of Interest: The authors declare no conflict of interest.

Appendix A. Test System Parameters

Table A1 presents the parameters of the test system.

Table A1. Parameters of the experimental setup of Figure 7.

DER Unit			
Parameter	Value	Rating	Manufacturer
Inverter power rating		20 kVA	Semikron
Switching frequency	10 kHz		
L_f, R_f	5 mH, 60 mΩ	25 A	Hammond
L_c, R_c	5 mH, 60 mΩ	25 A	Hammond
L_g, R_g	5 mH, 60 mΩ	25 A	Hammond
C_f	19 μF	240 V	Lab-Volt
Load			
R, L, C	8 Ω, 92.6 mH, 76 μF	500 W, 25 A, 240 V	Hammond, Lab-Volt
Grid and DC Source			
Voltage, Freq	86 V (rms-LL), 60 Hz	12 kVA	
DC Source	280 V	24 kW	
Controller			
OP5600	Real-time Simulator		OPAL-RT Technologies
OP8660	HIL Controller		OPAL-RT Technologies
UTSP			
ζ_1, ζ_2	0.4, 1.5		

Appendix B. Representation of Unbalanced Signals in the dq -frame

Consider an unbalanced three-phase signal, $x_{abc}(t)$, as

$$x_{abc}(t) = \begin{bmatrix} x_a(t) \\ x_b(t) \\ x_c(t) \end{bmatrix} = \begin{bmatrix} A_p \cos(\omega t + \delta_p) \\ A_p \cos(\omega t + \delta_p - 120) \\ A_p \cos(\omega t + \delta_p + 120) \end{bmatrix} + \begin{bmatrix} A_n \cos(\omega t + \delta_n) \\ A_n \cos(\omega t + \delta_n + 120) \\ A_n \cos(\omega t + \delta_n - 120) \end{bmatrix} + \begin{bmatrix} A_z \cos(\omega t + \delta_z) \\ A_z \cos(\omega t + \delta_z) \\ A_z \cos(\omega t + \delta_z) \end{bmatrix}$$

where A_p , A_n , and A_z are, respectively, the magnitudes of positive-, negative-, and zero-sequence, and δ_p , δ_n , and δ_z are the corresponding phase-angles. Applying the Park transformation with angle θ to the three-phase signal $x_{abc}(t)$ yields $x_d(t) = A_p \cos(\omega t - \theta + \delta_p) + A_n \cos(\omega t + \theta + \delta_n)$, $x_q(t) = A_p \sin(\omega t - \theta + \delta_p) - A_n \sin(\omega t + \theta + \delta_n)$, $x_0(t) = A_z \cos(\omega t + \delta_z)$. When $\omega t - \theta = \theta_0$, with θ_0 being a constant, the representation of the positive-sequence component of $x_{abc}(t)$ in the dq -frame will be constant components, while its negative-sequence component will oscillate at the double-frequency 2ω . Now, consider $x_d(t) = A + C \cos(2\omega t + \delta_d)$, $x_q(t) = B + D \cos(2\omega t + \delta_q)$, and $x_0(t) = 0$, where ω is the angular frequency, and the parameters A, B, C, D, δ_d , and δ_q are some constant real

numbers ($C \geq 0, D \geq 0$). Using the reference phase-angle $\theta(t) = \omega t$ and applying Park inverse transformation to $x_{dq0}(t)$ results in

$$\begin{aligned}x_a(t) &= A_a \cos(\omega t + \delta_a) + \frac{1}{2}C \cos(3\omega t + \delta_d) - \frac{1}{2}D \sin(3\omega t + \delta_q) \\x_b(t) &= A_b \cos(\omega t + \delta_b) + \frac{1}{2}C \cos(3\omega t + \delta_d - 120) - \frac{1}{2}D \sin(3\omega t + \delta_q - 120) \\x_c(t) &= A_c \cos(\omega t + \delta_c) + \frac{1}{2}C \cos(3\omega t + \delta_d + 120) - \frac{1}{2}D \sin(3\omega t + \delta_q + 120)\end{aligned}\quad (A1)$$

Thus, the conditions that eliminate the third harmonic are $C = D$ and $\delta_q = \delta_d + 90$.

References

- Camacho, A.; Castilla, M.; Miret, J.; Borrell, A.; de Vicuña, L.G. Active and reactive power strategies with peak current limitation for distributed generation inverters during unbalanced grid faults. *IEEE Trans. Ind. Electron.* **2014**, *62*, 1515–1525. [\[CrossRef\]](#)
- Nian, H.; Shen, Y.; Yang, H.; Quan, Y. Flexible grid connection technique of voltage-source inverter under unbalanced grid conditions based on direct power control. *IEEE Trans. Ind. Appl.* **2015**, *51*, 4041–4050. [\[CrossRef\]](#)
- Nejabatkhah, F.; Li, Y.W.; Wu, B. Control strategies of three-phase distributed generation inverters for grid unbalanced voltage compensation. *IEEE Trans. Power Electron.* **2015**, *31*, 5228–5241.
- Guo, X.; Liu, W.; Lu, Z. Flexible power regulation and current-limited control of the grid-connected inverter under unbalanced grid voltage faults. *IEEE Trans. Ind. Electron.* **2017**, *64*, 7425–7432. [\[CrossRef\]](#)
- Castilla, M.; Miret, J.; Camacho, A.; de Vicuña, L.G.; Matas, J. Modeling and design of voltage support control schemes for three-phase inverters operating under unbalanced grid conditions. *IEEE Trans. Power Electron.* **2014**, *29*, 6139–6150. [\[CrossRef\]](#)
- Rodriguez, P.; Timbus, A.V.; Teodorescu, R.; Liserre, M.; Blaabjerg, F. Flexible active power control of distributed power generation systems during grid faults. *IEEE Trans. Ind. Electron.* **2007**, *54*, 2583–2592. [\[CrossRef\]](#)
- Karimi, H.; Yazdani, A.; Iravani, R. Negative-sequence current injection for fast islanding detection of a distributed resource unit. *IEEE Trans. Power Electron.* **2008**, *23*, 298–307. [\[CrossRef\]](#)
- Dhar, S.; Dash, P.K. Performance analysis of a new fast negative sequence power injection oriented islanding detection technique for photovoltaic photovoltaic based voltage source converter based micro grid operation. *IET Gener. Transm. Distrib.* **2015**, *9*, 2079–2090. [\[CrossRef\]](#)
- Blaabjerg, F.; Teodorescu, R.; Liserre, M.; Timbus, A.V. Overview of control and grid synchronization for distributed power generation systems. *IEEE Trans. Ind. Electron.* **2006**, *53*, 1398–1409. [\[CrossRef\]](#)
- Du, X.; Gu, S.; Wang, G.; Tai, H.M.; Ji, Y. Simple current control method for three-phase VSC under unbalanced grid condition. *IET Power Electron.* **2018**, *11*, 1161–1168. [\[CrossRef\]](#)
- Shin, D.; Lee, K.J.; Lee, J.P.; Yoo, D.W.; Kim, H.J. Implementation of fault ride-through techniques of grid-connected inverter for distributed energy resources with adaptive low-pass notch PLL. *IEEE Trans. Power Electron.* **2014**, *30*, 2859–2871. [\[CrossRef\]](#)
- Mahamedi, B.; Eskandari, M.; Fletcher, J.E.; Zhu, J. Sequence-Based Control Strategy With Current Limiting for the Fault Ride-Through of Inverter-Interfaced Distributed Generators. *IEEE Trans. Sustain. Energy* **2018**, *11*, 165–174. [\[CrossRef\]](#)
- Zhao, X.; Guerrero, J.M.; Savaghebi, M.; Vasquez, J.C.; Wu, X.; Sun, K. Low-voltage ride-through operation of power converters in grid-interactive microgrids by using negative-sequence droop control. *IEEE Trans. Power Electron.* **2016**, *32*, 3128–3142. [\[CrossRef\]](#)
- Liserre, M.; Teodorescu, R.; Blaabjerg, F. Stability of photovoltaic and wind turbine grid-connected inverters for a large set of grid impedance values. *IEEE Trans. Power Electron.* **2006**, *21*, 263–272. [\[CrossRef\]](#)
- Midtsund, T.; Suul, J.; Undeland, T. Evaluation of current controller performance and stability for voltage source converters connected to a weak grid. In Proceedings of the 2nd International Symposium on Power Electronics for Distributed Generation Systems, Hefei, China, 16–18 June 2010, 382–388.
- Silwal, S.; Taghizadeh, S.; Karimi-Ghartemani, M.; Hossain, M.J.; Davari, M. An enhanced control system for single-phase inverters interfaced with weak and distorted grids. *IEEE Trans. Power Electron.* **2019**, *34*, 12538–12551. [\[CrossRef\]](#)
- Liu, W.; Blaabjerg, F.; Zhou, D.; Chou, S.F. Modified Instantaneous Power Control with Phase Compensation and Current-limited Function under Unbalanced Grid Faults. *IEEE J. Emerg. Sel. Top. Power Electron.* **2021**, *9*, 2896–2906. [\[CrossRef\]](#)
- Wu, W.; Liu, J.; Li, Y.; Blaabjerg, F. Individual Channel Design-Based Precise Analysis and Design for Three-Phase Grid-Tied Inverter with LCL-Filter under Unbalanced Grid Impedance. *IEEE Trans. Power Electron.* **2020**, *35*, 5381–5396. [\[CrossRef\]](#)
- Afshari, E.; Moradi, G.R.; Rahimi, R.; Farhangi, B.; Yang, Y.; Blaabjerg, F.; Farhangi, S. Control strategy for three-phase grid-connected PV inverters enabling current limitation under unbalanced faults. *IEEE Trans. Ind. Electron.* **2017**, *64*, 8908–8918. [\[CrossRef\]](#)
- Maccari, L.A.; Massing, J.R.; Schuch, L.; Rech, C.; Pinheiro, H.; Oliveira, R.C.; Montagner, V.F. LMI-based control for grid-connected converters with LCL filters under uncertain parameters. *IEEE Trans. Power Electron.* **2013**, *29*, 3776–3785. [\[CrossRef\]](#)
- Lai, N.B.; Kim, K.H. Robust control scheme for three-phase grid-connected inverters with LCL-filter under unbalanced and distorted grid conditions. *IEEE Trans. Energy Convers.* **2017**, *33*, 506–515. [\[CrossRef\]](#)
- Karimi, H.; Karimi-Ghartemani, M.; Sheshyekani, K. Robust control of three-phase voltage source converters under unbalanced grid conditions. *IEEE Trans. Power Electron.* **2019**, *34*, 11278–11289. [\[CrossRef\]](#)

23. Zarei, S.F.; Mokhtari, H.; Ghasemi, M.A.; Peyghami, S.; Davari, P.; Blaabjerg, F. Control of grid-following inverters under unbalanced grid conditions. *IEEE Trans. Energy Convers.* **2019**, *35*, 184–192. [[CrossRef](#)]
24. Yin, Y.; Vazquez, S.; Marquez Alcaide, A.; Liu, J.; Leon, J.I.; Wu, L.; Franquelo, L.G. Observer-Based Sliding Mode Control for Grid-Connected Power Converters under Unbalanced Grid Conditions. *IEEE Trans. Ind. Electron.* **2021**, *1*. [[CrossRef](#)]
25. Khalil, H.K. *Nonlinear Systems*, 3rd ed.; Prentice-Hall: Upper Saddle River, NJ, USA, 2002.
26. Li, J.; Zhang, Y.; Zhao, Y.; Ren, L.; Wang, J.; Liu, Y. An Improved Three-Stages Cascading Passivity-Based Control of Grid-Connected LCL Converter in Unbalanced Weak Grid Condition. *IEEE Access* **2021**, *9*, 89497–89506. [[CrossRef](#)]
27. Graungaard Taul, M.; Wang, X.; Davari, P.; Blaabjerg, F. Current Reference Generation Based on Next-Generation Grid Code Requirements of Grid-Tied Converters During Asymmetrical Faults. *IEEE J. Emerg. Sel. Top. Power Electron.* **2020**, *8*, 3784–3797. [[CrossRef](#)]
28. Guan, L.; Yao, J.; Liu, R.; Sun, P.; Gou, S. Small-Signal Stability Analysis and Enhanced Control Strategy for VSC System during Weak-Grid Asymmetric Faults. *IEEE Trans. Sustain. Energy* **2021**, *1*. [[CrossRef](#)]
29. Davison, E.; Ferguson, I. The design of controllers for the multivariable robust servomechanism problem using parameter optimization methods. *IEEE Trans. Autom. Control.* **1981**, *26*, 93–110. [[CrossRef](#)]
30. Sadabadi, M.S.; Haddadi, A.; Karimi, H.; Karimi, A. A Robust Active Damping Control Strategy for an LCL-Based Grid-Connected DG Unit. *IEEE Trans. Ind. Electron.* **2017**, *64*, 8055–8065. [[CrossRef](#)]
31. Safonov, M.; Athans, M. Gain and phase margin for multiloop LQG regulators. *IEEE Trans. Autom. Control.* **1977**, *22*, 173–179. [[CrossRef](#)]
32. Lin, F. *Robust Control Design: An Optimal Control Approach*; John Wiley & Sons: Chichester, UK, 2007.
33. Sadabadi, M.S.; Peaucelle, D. From static output feedback to structured robust static output feedback: A survey. *Annu. Rev. Control* **2016**, *42*, 11–26. [[CrossRef](#)]
34. Ebihara, Y.; Peaucelle, D.; Arzelier, D. *S-Variable Approach to LMI-Based Robust Control*, 1st ed.; Springer: London, UK, 2015.
35. Lofberg, J. YALMIP: A toolbox for modeling and optimization in MATLAB. In Proceedings of the 2004 IEEE International Conference on Robotics and Automation (IEEE Cat. No.04CH37508), Taipei, Taiwan, 2–4 September 2004; pp. 284–289. [[CrossRef](#)]
36. MOSEK ApS. *The MOSEK Optimization Toolbox for MATLAB Manual. Version 9.0.*; 2019.